JOURNAL OF GEOPHYSICAL RESEARCH, VOL. 114, A10302, doi:10.1029/2009JA014087, 2009

First results of the limb imaging of 630.0 nm airglow using FORMOSAT-2/Imager of Sprites and Upper Atmospheric Lightnings

P. K. Rajesh,[1] J. Y. Liu,[1] C. Y. Chiang,[2] A. B. Chen,[2] W. S. Chen,[1] H. T. Su,[2] R. R. Hsu,[2] C. H. Lin,[2] M.-L. Hsu,[2] J. H. Yee,[3] and J. B. Nee[4]

Received 19 January 2009; revised 2 June 2009; accepted 15 June 2009; published 9 October 2009.

[1] This is the first report of the most comprehensive 630.0 nm airglow limb images taken using Imager of Sprites and Upper Atmospheric Lightnings (ISUAL) onboard FORMOSAT-2. The limb scans reveal two distinct airglow layers: the upper one corresponds to the thermospheric $O(^1D)$ emission and the lower one corresponds to the OH (9–3) emissions. Sequences of such observations are combined to generate altitude-latitude maps of the emissions, which reveal intensity enhancements of both the layers at certain locations where they often appear to be linked/joined vertically. A detailed analysis of the location and occurrence of the enhancements in the entire observations, together with simulations of the emissions suiting the ISUAL limb geometry are carried out to understand the causes and related processes.

Citation: Rajesh, P. K., et al. (2009), First results of the limb imaging of 630.0 nm airglow using FORMOSAT-2/Imager of Sprites and Upper Atmospheric Lightnings, *J. Geophys. Res.*, *114*, A10302, doi:10.1029/2009JA014087.

1. Introduction

[2] Airglow emissions have been widely used to understand the chemical and dynamical processes controlling the state of the upper mesosphere and lower thermosphere [*Chakrabarti*, 1998]. By monitoring selected emissions as a function of space and time, one can study such processes and their temporal and spatial evolutions. The atomic oxygen emission at 630.0 nm is one of the most prominent lines in the airglow spectrum that has been extensively studied using ground based photometers [*Greenspan*, 1966; *Nelson and Cogger*, 1971; *Bittencourt and Sahai*, 1979; *Herrero and Meriwether*, 1980; *Burnside and Tepley*, 1990; *Chu et al.*, 2005], and all sky cameras [*Weber et al.*, 1978; *Mendillo and Baumgardner*, 1982; *Sahai et al.*, 1994, 2000; *Fagundes et al.*, 1999; *Taylor et al.*, 1997; *Kelley et al.*, 2002; *Sinha et al.*, 2003; *Martinis et al.*, 2003; *Mukherjee*, 2003; *Pimenta et al.*, 2003; *Makela et al.*, 2004; *Mendillo et al.*, 2005; *Rajesh et al.*, 2007]. The major source of the 630.0 nm in the nighttime ionosphere is the dissociative recombination and its intensity is proportional to the plasma density [*Peterson et al.*, 1966; *Link and Cogger*, 1988]. Also, the emission is sensitive to *F* layer height variations [*Nelson and Cogger*, 1971; *Bittencourt and Sahai*, 1979; *Herrero and Meriwether*, 1980]. These features make the 630.0 nm airglow an ideal tracer of ionospheric variations and thermospheric-ionospheric interaction. In addition to this atomic oxygen emission, the 630.0 nm region also have a spectral contribution from the mesospheric heights from the OH(9–3) vibrational transitions at 628.7, 629.8, and 630.6 nm [*Burnside et al.*, 1977; *Mende et al.*, 1993].

[3] In order to study the thermospheric-ionospheric phenomena and its variability, long-term airglow observations are required. Space shuttle or satellite programs are best suitable for such investigations. The earlier space shuttle measurements [*Torr et al.*, 1985; *Swenson et al.*, 1989] had only limited spectral coverage. *Mende et al.* [1993] provided the limb spectrum of the visible airglow covering altitudes below 150 km using observations made onboard a space shuttle orbiting at 250 km. Their 630.0 nm results showed strong OH(9–3) contribution. One of the successful missions that made nadir integrated measurements at 630.0 nm was Orbital Geophysical Observatory (OGO 4 and 6) launched in the sixties, which revealed several interesting features such as the longitudinal patterns in the 630.0 nm distribution and its relationship with meridional wind [*Thuillier et al.*, 1976]. Similarly, ISIS-II mission carried a red line photometer that made 630.0 nm mapping from the spin-stabilized spacecraft [*Shepherd et al.*, 1973]. The WIND Image Interferometer (WINDII) onboard the Upper Atmospheric Research Satellite (UARS) also provided a few OI 630.0 nm limb-viewing observations [*Thuillier et al.*, 2002], confirming the OGO results.

[4] There had been no satellite mission after WINDII (1991–2003) to measure the 630.0 nm emission until the launch of FORMOSAT-2 in May 2004, which is equipped with Imager of Sprites and Upper Atmospheric Lightnings (ISUAL), featuring a filter-wheel-controlled camera including the 630.0 nm band [*Chern et al.*, 2003]. Though the ISUAL is primarily designed for the limb-viewing studies

[1]Institute of Space Science, National Central University, Chung-Li, Taiwan.
[2]Department of Physics, National Cheng Kung University, Tainan, Taiwan.
[3]Johns Hopkins University Applied Physics Laboratory, Laurel, Maryland, USA.
[4]Department of Physics, National Central University, Chung-Li, Taiwan.

0148-0227/09/2009JA014087$09.00

of transient luminous events (TLE) induced by thunderstorm activities [*Kuo et al.*, 2005; *Adachi et al.*, 2006; *Liu et al.*, 2006], it also provides the limb images of upper atmosphere at different wavelengths as the FORMOSAT-2 tracks from the South Pole to the North Pole in the night hemisphere. Depending on the satellite pitch angle, ISUAL could image an altitude range between 30 km to over 330 km while also providing a significant latitudinal coverage. Currently it might be the only space-borne instrument taking the limb images of the upper atmosphere in the visible band.

[5] This is the first report of the ISUAL observations of the upper atmospheric visible airglow, especially at 630.0 nm. In this work we describe the 630.0 nm ISUAL images, revealing latitudinal distribution of the emission, enhancements and intensity variations, and contribution from different altitudes. Detailed simulations of the emissions corresponding to the instrument viewing geometry are carried out to explain the observed features, in particular the enhancements and their altitudinal joining.

2. Observation

[6] FORMOSAT-2 makes 14 revolutions around the Earth per day from its sun-synchronous, circular, polar orbit (inclination 98.99°) at an altitude of about 891 km. There are three sensor packages in the ISUAL payload including an intensified CCD imager, a six-channel spectrophotometer, and a dual-band array photometer. In this work the 630.0 ± 3.5 nm CCD images taken during the period January 2007 to March 2008 are used. The imager has a horizontal field of view (FOV) of 20° and a vertical FOV of 5°, with a corresponding pixel dimension of 516 × 128. In addition to the 630.0 nm channel chosen for the present study, the CCD imager can also record emissions at 5 other wavelength channels (for further details refer to *Chern et al.* [2003]).

[7] Figure 1a displays the typical viewing geometry of the ISUAL. The tangent heights of the lines of sight from the bottom and top pixels of a given column cover an altitudinal range from ~30 km to ~330 km, which include the $O(^1D)$ 630.0 nm emission from the thermosphere as well as the OH(9–3) bands from the mesosphere. Both these emissions are within the ISUAL bandwidth. Figure 1b gives the typical satellite trajectories of the observations in 2007 together with the ground projection of the FOV for the track scanned in the night of 29 September 2007. The imager views the Earth limb looking to the right as the satellite is orbiting northward. Thus, a single frame is the line of sight integration of the emissions spanning a wide range of longitudes, where the vertical and horizontal pixels provide the altitudinal and latitudinal coverage. An image is taken approximately every 30 s with about 40/41 such frames per track. It can be seen from Figure 1b that the tangent plane is about 2 h (~30° to the East) ahead of the satellite ground projection. There are 14 such tracks at different longitude sectors, generally covering the latitudes between 40°S to 60°N in the observations taken in 2007.

[8] Figure 1c shows a sample 630.0 nm limb image taken at about 2342 UT on 27 September 2007 corresponding to the scan highlighted in black in Figure 1b. The vertical pixels cover about 300 km of altitude and the horizontal pixels enclose a latitude region of about 10°, where the intensity at each pixel is the integrated value along the lines of sight passing through a range of longitudes and altitudes. The image reveals two distinct layers of the emission, centered at different altitude levels. The upper layer is wide, but is not seen over the entire latitudes covered by the horizontal pixels. By contrast, the lower layer is narrow and exists throughout the horizontal FOV of the image. The arc shape of the layers follows the curvature of the Earth. As depicted in Figure 1a, the two possible sources of the 630.0 nm airglow within the FOV and band width of the ISUAL that can give rise to the observed layers are the $O(^1D)$ state and the OH(9–3) transitions.

[9] Figure 2 displays a sequence of 28 selected ISUAL images recorded in the night of 27 September 2007, after projecting each pixel to the corresponding tangent height and latitude. Each frame corresponds to the individual latitudinal scans of ISUAL, covering about 10° of latitude with a considerable overlap in successive images. All such latitudinal scans taken over the satellite track in Figure 1b are merged together in Figure 2 (bottom). This altitude-latitude map of the emission is constructed by combining about 40 images recorded during 2328–2347 UT, in this night. Together, these frames image the region between 20°S to 50°N. The individual limb scans as well as the combined image confirm that the upper layer is located in the 200–300 km region where the $O(^1D)$ state is usually populated through recombination reactions, giving rise to the 630.0 nm emission. The lower layer is seen centered around 85–90 km altitude, which coincides with the peak of the OH bands. Henceforth, the upper layer is referred to as $O(^1D)$ layer and the lower layer as OH(9–3) layer.

[10] It can be seen from the limb images in Figure 2 that the $O(^1D)$ and the OH(9–3) emissions exhibit spatial variations. The $O(^1D)$ layer is seen only over a limited range of latitudes between 0 and 10°N peaking near 4°, and a slight intensification near 50°N, while the OH(9–3) layer appears in all the images. When there is an enhancement of the $O(^1D)$ emission, the OH(9–3) layer also show a corresponding increase in its intensity. Note that there is a vertical joining of the $O(^1D)$ and the OH(9–3) enhancements in Figure 2. This must be caused by the distribution of the intensities of the two emissions along the lines of sight (Figure 1a). The lines of sight from the upper most pixels do not traverse the regions of either the $O(^1D)$ or the OH(9–3) emission, and hence result in the lesser intensities of these pixels. The $O(^1D)$ and the OH(9–3) layers are seen at those pixels whose lines of sight reside longer distance in these emissions near their tangent point. In the region between the two layers the intensity comes from the lines of sight that penetrate through the $O(^1D)$ layer above and/or below the corresponding tangent height. This contributes in the vertical linking of the layers. Similarly, the lines of sight corresponding to the lower pixels intercept small portions of the OH(9–3) and the $O(^1D)$ layers, and give rise to the OH(9–3) enhancement as well as the intensity seen at altitudes much below OH(9–3) emission peak.

[11] Figure 3 displays a set of selected altitude-latitude maps of the 630.0 nm emission taken over different satellite tracks that exhibit typical enhancement features and vertical linking. All the images show the OH(9–3) layer with

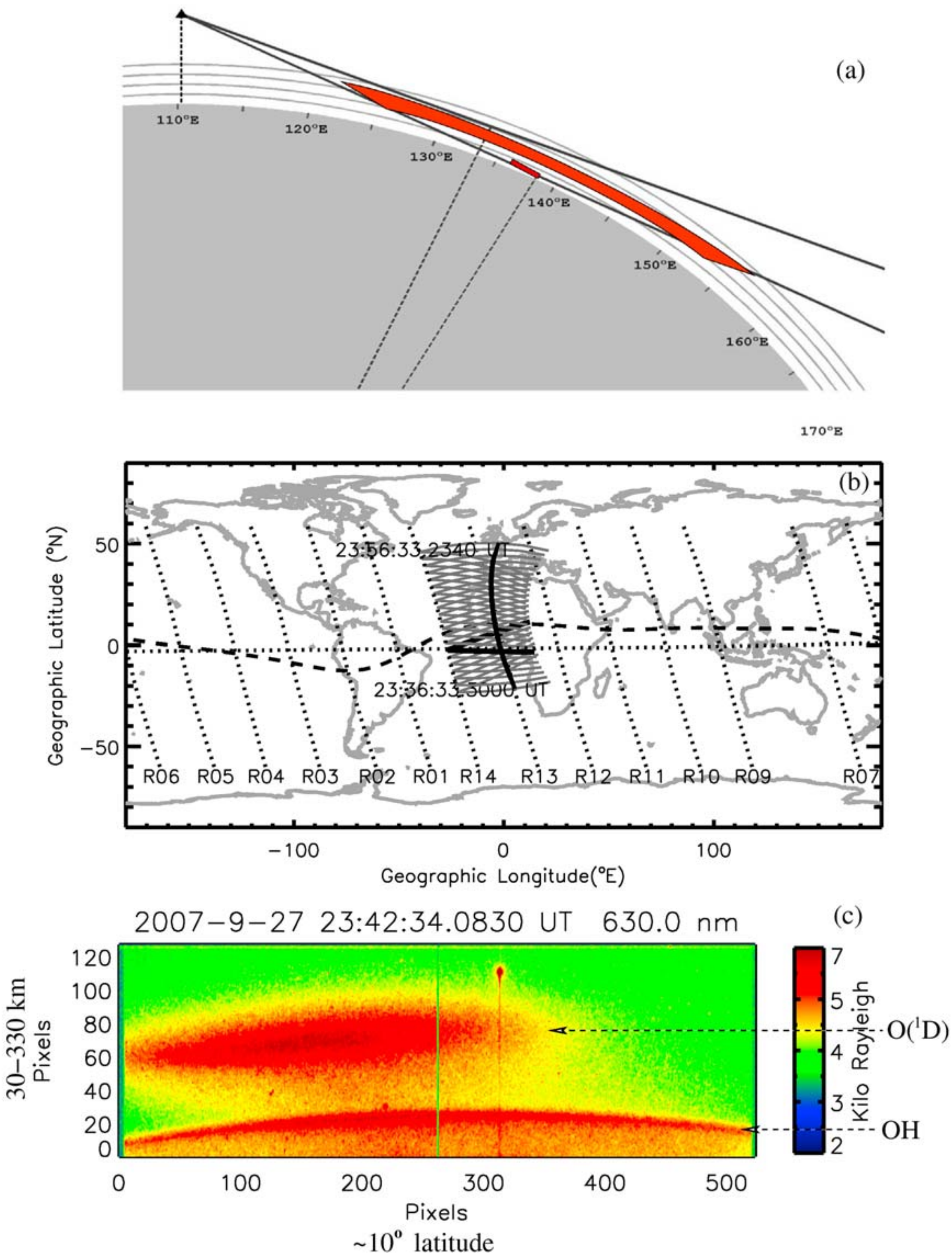

Figure 1. The ISUAL viewing geometry. (a) The arcs are drawn every 100 km above the Earth's surface. The dark solid lines denote the lines of sight that cover the entire vertical FOV, and the tangent points are the locations where the dashed lines intercept these solid lines. The tangent heights cover a region between 30 and 300 km altitudes. The shades in red color represent airglow emissions within the FOV. (b) The ground projection of the satellite tracks (R01–R14) for the observations in 2007. The lines of sight for a typical limb observation along R14 are shown with the gray (and for one highlighted in black) lines. The time in UT (universal time) denotes the beginning and end of observations. The black solid line parallel to the orbit gives the ground projection of the tangent point plane and the dashed line is the geomagnetic equator. (c) A typical ISUAL image taken in the night of 27 September 2007, corresponding to the case where the lines of sight are highlighted in black in Figure 1b. The *x* and *y* axes are in pixel coordinates.

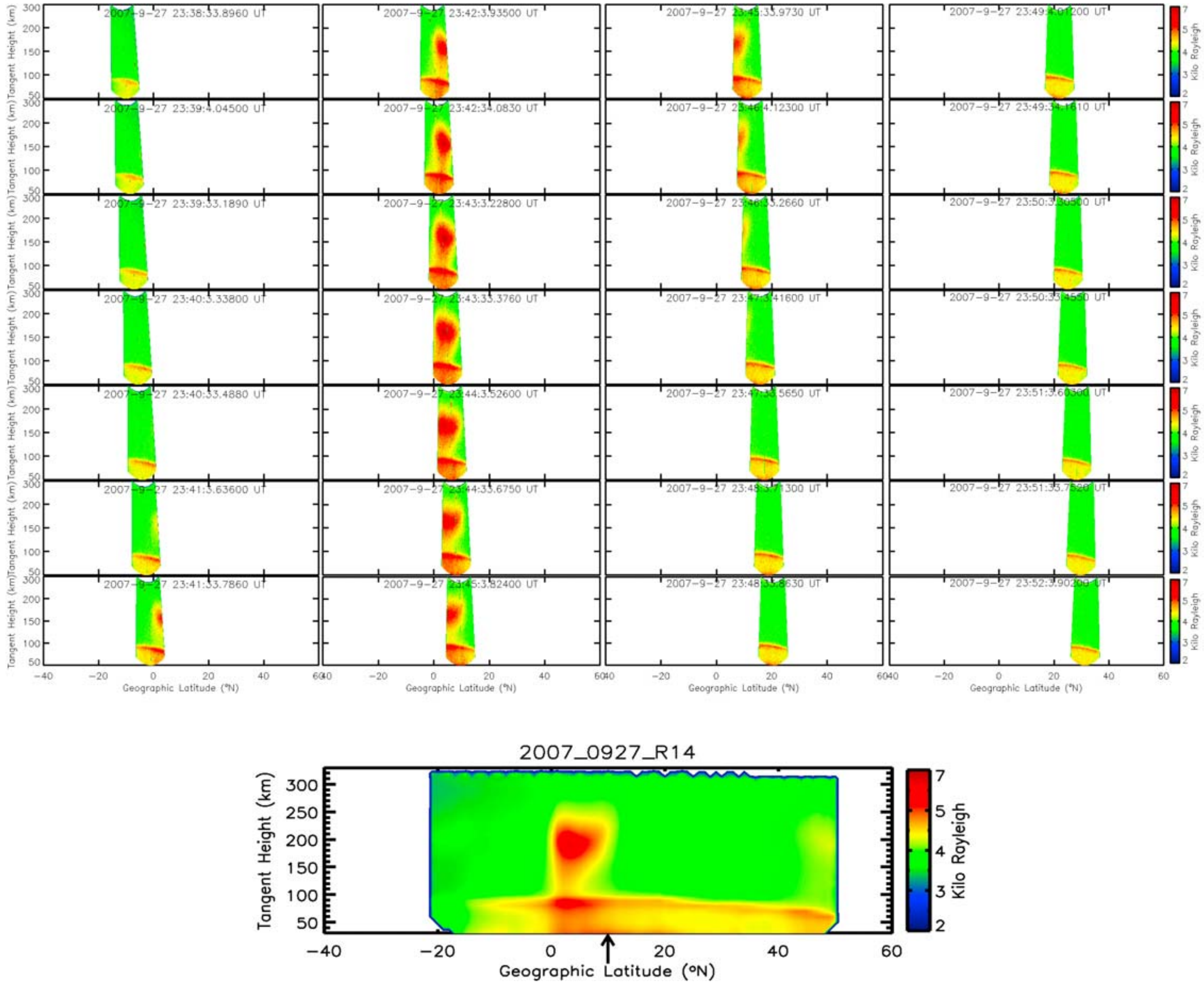

Figure 2. (top) The ISUAL images taken on 27 September 2007 after projecting each pixel to the corresponding tangent point latitude and height. The trajectory and viewing geometry of the satellite are the same as in Figure 1b. The order of the frames are from top to bottom and then left to right. (bottom) The individual latitudinal scans are merged together. The arrow given in Figure 2 (bottom) denotes the geomagnetic equator.

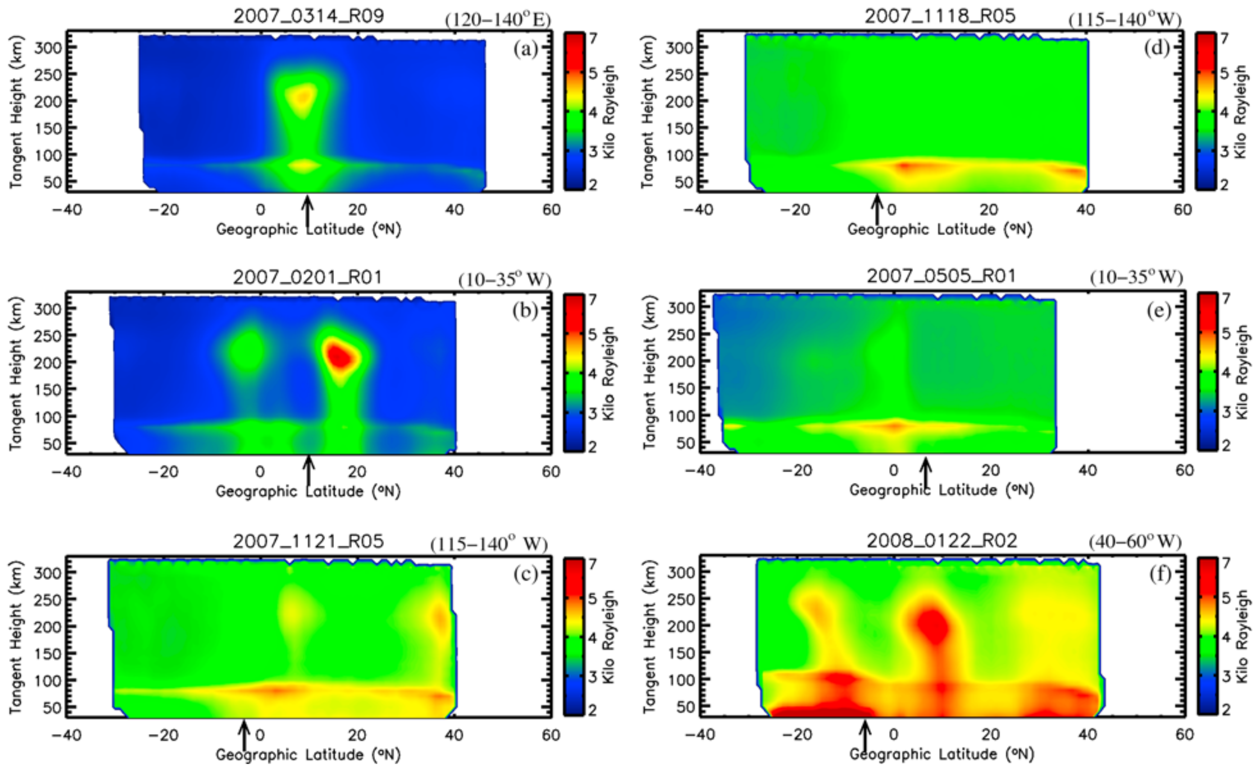

Figure 3. A set of selected ISUAL images. The title of each gives the date of observation, the satellite track, as well as the longitudes covered at the tangent plane. The arrow denotes the geomagnetic equator.

enhancements over it at certain latitudes, while the O(^{1}D) emission basically appear as patches of intensity peaks over a weak background. The O(^{1}D) intensity in the nighttime is a function of the electron density as well as the height of the *F* layer. Traveling ionospheric disturbances (TID) and meridional winds are two possible candidates that can raise or lower the plasma along the field lines and modify the emission, in addition to height variations that could be caused by electric fields. The O(^{1}D) intensity in Figures 3a–3f could in fact be explained on the basis of seasonal meridional winds that have less influence in equinoxes, but could enhance the emission in winter hemisphere [*Thuillier et al.*, 1976, 2002; *Wiens et al.*, 2004]. Figure 3a represents the equinox condition with the emission increasing toward equator, while Figures 3b–3f correspond to the northern winter season where the intensity appear stronger than that in the corresponding southern hemisphere. In Figure 3e, the emission in the southern hemisphere, which is the winter hemisphere, appears to be brighter.

[12] Thus, the overall O(^{1}D) intensity gradients in Figure 3 could be understood on the basis of the neutral winds, and the peaks at or near the equator in the emission could be related to nighttime background electron density. Most of the OH(9–3) peaks are most likely the contribution from the line of sight integration of the corresponding O(^{1}D) peaks. However, there are two midlatitude O(^{1}D) peaks, one between 35 and 40°N in Figure 3c and the other one between 25 and 40°N in Figure 3f, which are unlikely to be caused by background electron density. In the case of Figure 3c there were slightly disturbed geomagnetic conditions with the kp values more than 3 for three consecutive periods and Dst index below −50 nT. There was a minor geomagnetic storm in the previous night (20 November 2007), with Dst about −71 nT. For the enhancement in Figure 3f, there is no any geomagnetic disturbance during this period. Similarly, in Figure 3d, there are two OH(9–3) peaks without any significant O(^{1}D) peaks, indicating that the enhancement is related to an increase in the OH(9–3) emission itself and not the result of line of sight integration. Also, there is a strong layer of enhanced emission below 50 km altitude in Figure 3f, with no such strong or extended peak at higher altitudes. Moreover, the vertical joining in this case appears to be tilted. Note that the lines of sight corresponding to this observation pass through the South Atlantic Anomaly (SAA) region.

3. Simulation

[13] As illustrated above, the ISUAL observations sometimes reveal enhancements of O(^{1}D) and OH(9–3) emissions during disturbed and quiet periods, and also over the SAA region. Such enhancements could be related to TID's, precipitation of charged particles and/or neutral atoms, tides or gravity waves. In some cases, the vertical joining due to line of sight integration appears to be tilted. To understand the cause mechanism of such enhancement features and joining, detailed simulations of O(^{1}D) and OH(9–3) emissions are carried out for the observations taken on 27 September 2007. On the basis of the viewing geometry in Figure 1, the latitude, longitude, and altitude of different points along the line of sight for each pixel is determined. International Reference Ionosphere (IRI-07) model [*Bilitza*, 2001] and Mass Spectrometer Incoherent Scatter Radar (NRLMSISE-00) model [*Hedin*, 1991] are

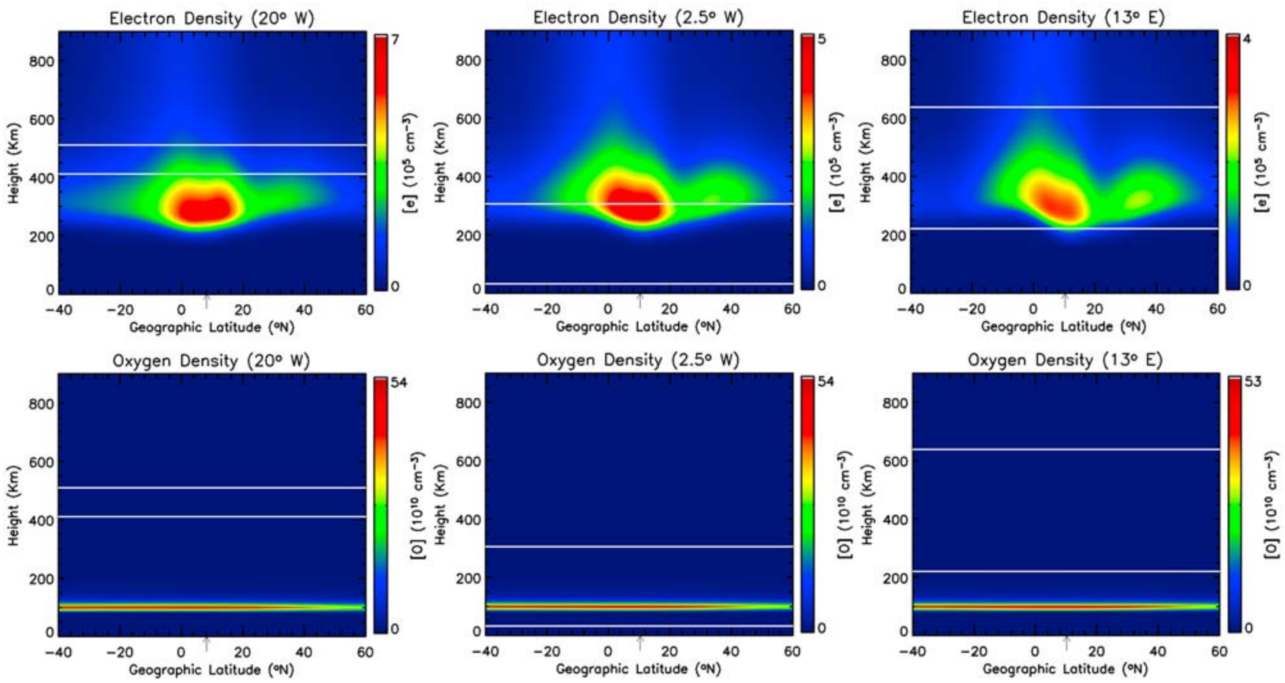

Figure 4. The input electron density and the atomic oxygen density at three different longitudes around midnight along the lines of sight used in the simulations. Figure 4 (middle) is close to the tangent plane. The white horizontal lines parallel to the *y* axis (latitude) are the top and bottom altitudes covered by the lines of sight at the respective longitudes. The arrow denotes the geomagnetic equator.

used to obtain the plasma and neutral parameters at these locations corresponding to the time of observations, and volume emission rates of the O(^{1}D) and the OH(9–3) transitions are calculated. The O(^{1}D) emission is simulated using the coefficients given by *Link and Cogger* [1988], while the OH(9–3) simulations are based on *Makhlouf et al.* [1995]. The limb images are reconstructed by integrating the volume emissions over a longitude region of about 45°, in approximately 1° segments, so that the major source regions of the emissions are well within the volume used for calculations. Figure 4 displays the background input electron density as well as atomic oxygen density used for the simulations at three different longitudes, one near the satellite location, one at the tangent plane, and one near the end of the lines of sight. The electron density shows a peak right above the magnetic equator, and appears to weaken from the satellite location along the lines of sight. On the other hand, the atomic oxygen density is concentrated over a narrow altitude region in between 80 and 150 km, and has little spatial variation.

[14] To confirm whether the emission peaks could be caused by some precipitating energetic particles, which increase plasma as well as neutral densities, or the effect of traveling disturbances producing localized plasma enhancement, the simulations are also repeated by introducing artificial enhancements in the densities at different altitudes. First, the plasma density is increased in between 200 and 300 km altitudes to see the effect of any ionization by some external particles or dynamics in this region. Similarly, the atomic oxygen density is increased in between 60 and 95 km in order to reproduce the result of possible neutral density modification in this region. The combined effect of these two cases is also simulated. The simulations are also done with the artificial enhancements of plasma density, atomic oxygen density, as well as the combination of the two, over all the altitudes covered by the lines of sight. In addition to these, the entire sequences of artificial density enhancements are repeated for a different latitude scan where a slight equatorward shift is given to the satellite yaw angle. This is to check if satellite attitude plays any role in producing the tilted joining.

[15] Results of the simulations without applying any density enhancements are given in Figure 5, where a sequence of selected 28 individual scans as well as the combined image of the entire simulations is displayed. The simulations not only show both the O(^{1}D) and OH(9–3) layers, but reproduce the enhancements as well as their joining. The general features revealed in the individual scans as well as the combined image are similar to that seen in the observations (Figure 2), though the location of the enhancement is different. This could be due to the differences in the actual atmospheric density distribution and other background parameters from those used for the simulations.

[16] Figure 6 gives the results of repeating the simulations by introducing artificial enhancement in plasma and neutral densities between 25 and 35°S latitudes. Figure 6a corresponds to the case where the plasma density is enhanced by a factor of 10 in between 200 and 300 km altitude regions. This creates a very strong enhancement of both the O(^{1}D) and the OH(9–3) layers, as well as their vertical joining. This is similar to the midlatitude O(^{1}D) enhancements seen in the observations. Figure 6b is the result of increasing the

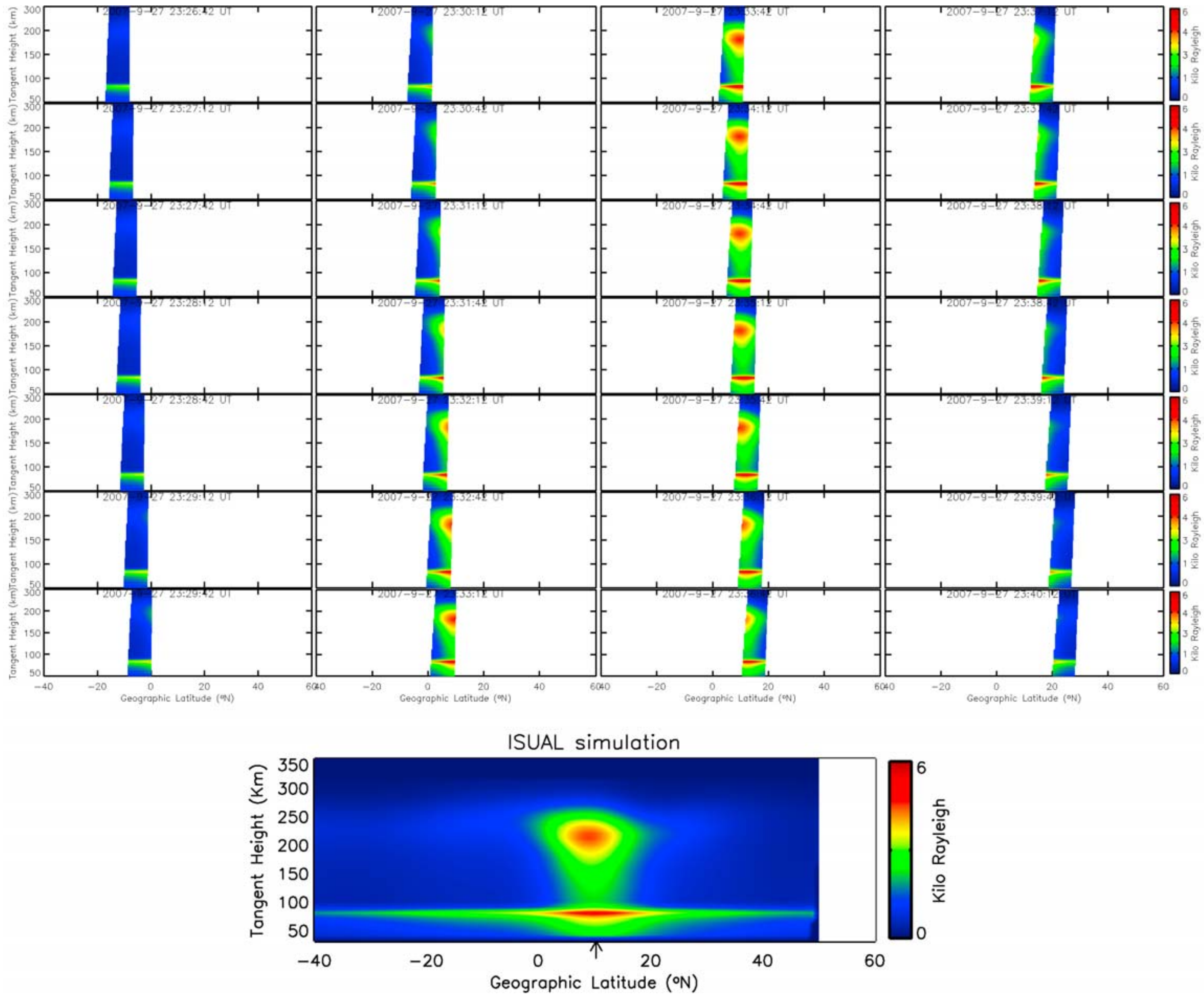

Figure 5. Results of ISUAL simulations. (top) Tangent height-latitude projections of selected 27 scans and (bottom) the combination of all individual scans are given. The order of the individual scans are from top to bottom and then left to right. The simulations are carried out for the observations on 27 September 2007, corresponding to the trajectory and viewing geometry in Figure 1b. The arrow given in Figure 5 (bottom) denotes the geomagnetic equator.

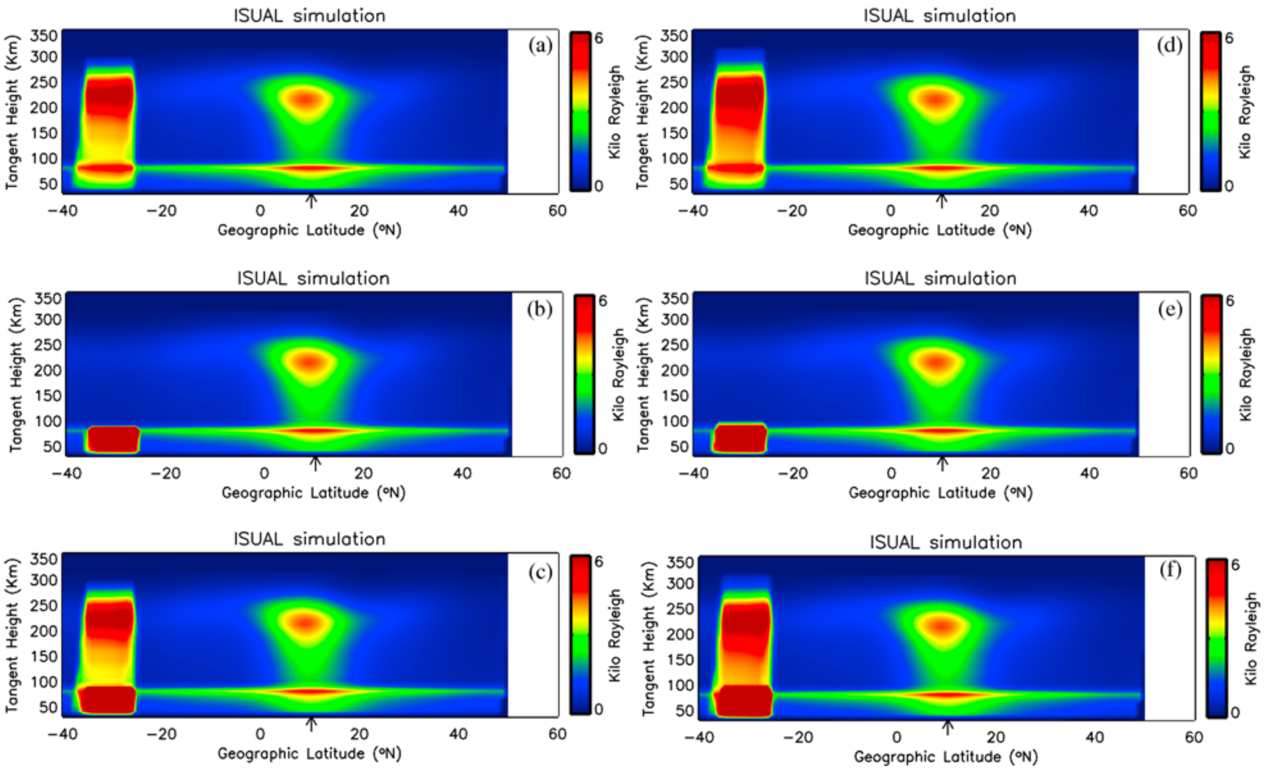

Figure 6. Results of simulations with artificial density enhancements between 25 and 35°S latitudes. (a) Plasma density ([O^+] and [e]) enhanced by 10 times between 200 and 300 km. (b) Atomic oxygen enhanced by 10 times between 60 and 95 km. (c) Combination of Figures 6a and 6b. (d–f) Similar to Figures 6a, 6b, and 6c but the enhancements are applied over all the altitudes in each case. The arrow denotes the geomagnetic equator.

atomic oxygen density between 60 and 95 km altitudes by a factor of 10, keeping other parameters unchanged. This produces a strong layer of OH(9–3) emission in these latitudes that extends down to 50 km altitude. Note that there is no corresponding enhancement of the O(^{1}D) layer or any vertical joining in this simulation. Figure 6c is the combined effect of the above two simulations (plasma density enhanced between 200 and 300 km and oxygen density between 60 and 95 km), which again shows strong enhancement of both the layers as well as their vertical joining.

[17] Figures 6d–6f in Figure 6 are similar to Figures 6a–6c, except that the density enhancements are introduced over all the altitudes intercepted by the lines of sight passing through 25–35°S latitudes. The results do not reveal any significant differences in the enhancement or joining features from those in Figures 6a–6c. Similar simulations as described above were repeated by introducing artificial density enhancements between 25 and 35°N latitudes and the results are arranged in Figure 7. There is an equatorward shift for the satellite yaw angle in this case. The noticeable difference here is that there is a slight shift in the latitudes of the peaks in the O(^{1}D) and the OH(9–3) layers when the plasma density is increased between 200 and 300 km altitudes, reproducing the tilted joining feature.

[18] The results in Figures 6 and 7 confirm that the equatorial enhancement in O(^{1}D) is related to the background plasma density and that the midlatitude peaks in O(^{1}D) emission and a corresponding enhancement of OH(9–3) from line of sight integration could be produced if there is an increase in the plasma density in the 200–300 km region. Also, the OH(9–3) peaks without any O(^{1}D) enhancement are possible if the atomic oxygen density is increased in the region below 100 km. The tilted joining is caused by a slight equatorward yaw angle in the instrument view while taking those limb scans. As a result, the lines of sight from pixels corresponding to different tangent heights meet the emission at different latitudes, producing a shift in the locations of the O(^{1}D) and OH(9–3) enhancements and hence the tilted joining.

4. Discussion and Conclusion

[19] The observations and simulations demonstrate the role of the ISUAL viewing geometry, and the increase of plasma and/or oxygen density in producing the enhancements and the joining features. The vertical joining or linking of the emissions is an artifact of the geometry, as the lines of sight that contribute to the intensity at each pixel traverse either the O(^{1}D) or OH(9–3) emissions or both. Depending on the satellite attitude, this joining could appear tilted. The geometry is also responsible for the OH(9–3) enhancement, which is associated with a corresponding O(^{1}D) enhancement and vertical joining. However, the cases of OH(9–3) enhancements without O(^{1}D) are confirmed to be caused by an increase of atomic oxygen densities below 100 km region in the simulations. In other words, an O(^{1}D) enhancement caused by enhanced plasma

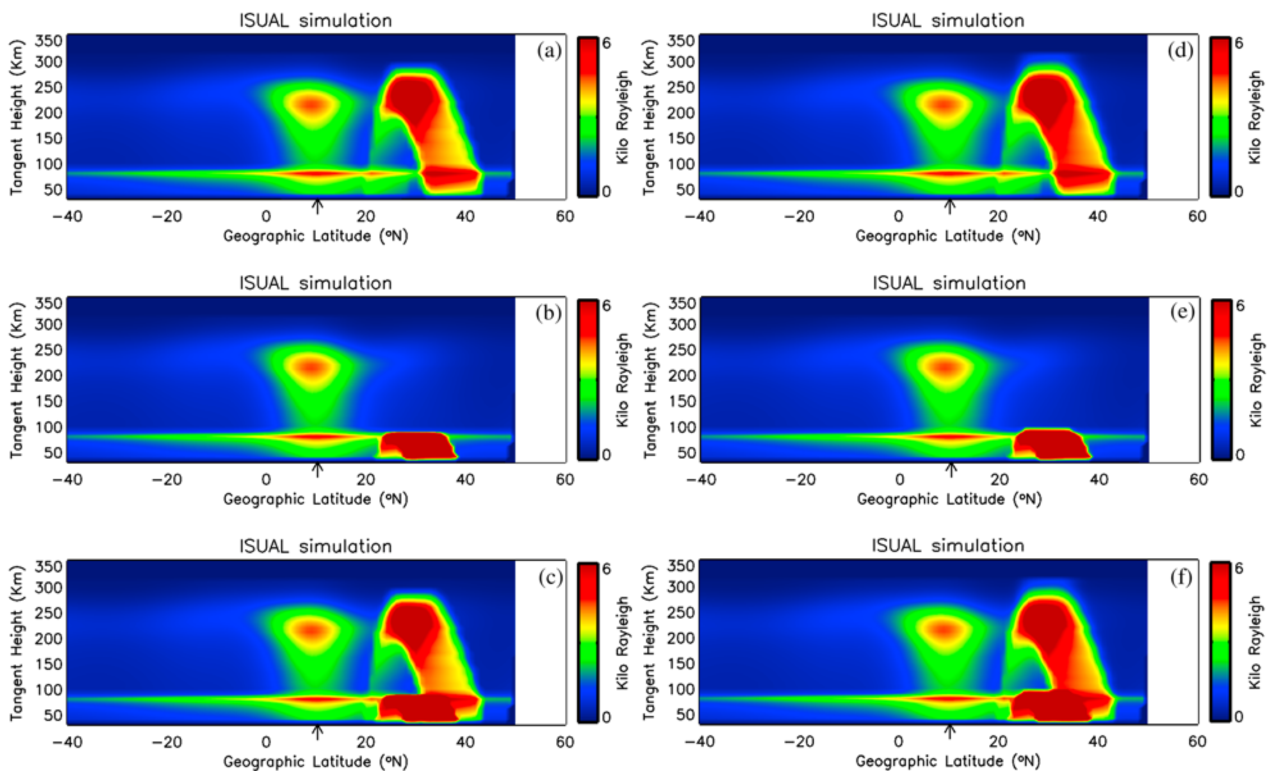

Figure 7. Same as in Figure 6, but the density enhancement is applied between 25 and 35°N.

density can result in the vertical joining as well as a corresponding enhancement of the OH(9–3) layer, while an enhancement of the OH(9–3) emission due to increase in atomic oxygen density do not produce any joining feature or enhancement of the O(^{1}D) emission.

[20] To address the origin of the enhancements, detailed analysis of their location of appearance in the observations during 2007–2008 are carried out and their occurrence in the O(^{1}D) and OH(9–3) emissions as a function of geomagnetic latitude is given in Figure 8. About 57% of the observations showed O(^{1}D) enhancements, while about 65% of the cases had OH(9–3) enhancements. Majority of the enhancements are seen right above geomagnetic equator. The O(^{1}D) enhancements in these nighttime observations could come from the greater electron density near the magnetic equator at these local times. Meridional winds play important role in organizing plasma along the geomagnetic field lines and result in an increase and decrease of the O(^{1}D) emission [*Colerico et al.*, 1996; *Burnside and Tepley*, 1990; *Thuillier et al.*, 1976, 2002; *Wiens et al.*, 2004]. Though the Equatorial Ionization Anomaly generally weakens toward midnight, any remaining ionization could also contribute. During geomagnetic disturbances, precipitation of energetic charged particles could increase ionospheric plasma density [*Baker et al.*, 1987; *Lin and Yeh*, 2005; *Dmitriev and Yeh*, 2008], and hence the O(^{1}D) intensity, especially in the midlatitudes. TID's, often associated with geomagnetic activity, also modify plasma density [*Bowman*, 1977; *Hocke and Schlegel*, 1996; *Shiokawa et al.*, 2003]. Another possible external source of ionization that could produce the O(^{1}D) enhancements in the midlatitudes is the energetic neutral atom (ENA) precipitation [*Torr and Torr*, 1984; *Roelof*, 1987]. Though ENA induced airglow enhancements are noticed during geomagnetic disturbances [*DeMajistre et al.*, 2005], *Tinsley et al.* [1994] reported such events under quiet magnetic conditions at middle and low latitudes.

[21] Most of the observed OH(9–3) enhancements in Figure 8 are the result of the line of sight integration of the corresponding O(^{1}D) enhancements. However, the

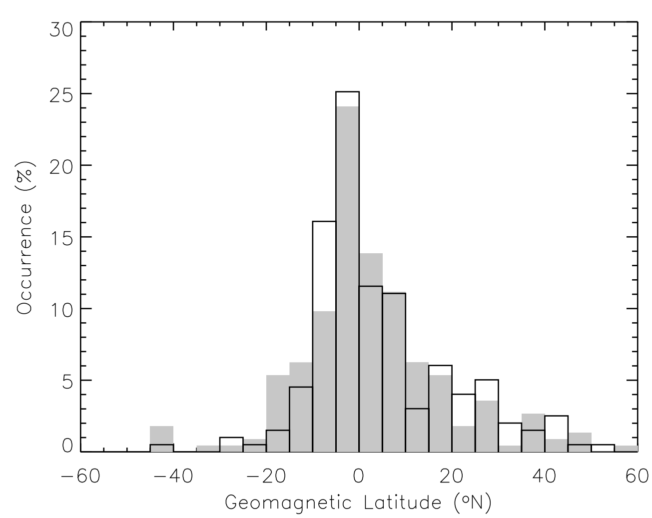

Figure 8. The distribution of the enhancements as a function of the geomagnetic latitude. The occurrence is estimated for every 5° latitude bin. The dark solid line stands for O(^{1}D), and the region in gray shade for OH(9–3) enhancements. About 215 enhancement events were used for the statistics in each case.

events of OH(9–3) enhancements in the absence of any corresponding O(^{1}D) enhancement indicate the response of photochemistry to mesospheric atomic oxygen density modifications. Note that the lines of sight contributing to the integrated images described here mainly intersect the 2200 local time to postmidnight sectors. Downward transport of atomic oxygen due to increased eddy diffusion by tides or gravity waves has been shown to enhance the OH emission around midnight, especially in winter months [*Takahashi et al.*, 1977]. Dynamics influence on the atomic oxygen density, affecting airglow emissions, is demonstrated by *Shepherd et al.* [1999]. Diurnal and semidiurnal tide also could significantly change the OH intensity [*Takahashi et al.*, 1984, 1999; *Scheer and Reisen*, 1998; *Zhang et al.*, 2001; *Lopez-Gonzalez et al.*, 2005]. Though, tides and gravity waves could modify the OH(9–3) emission, producing peaks even in the absence of any corresponding O(^{1}D) peaks, the strong emission layer below 50 km seen over SAA region is unlikely by such processes. One could speculate that ENA precipitation could increase the atomic oxygen density at altitudes below 100 km, and produce such OH(9–3) enhancements, depending on the energy of the precipitating particles. However, detailed investigations of the input energy and flux are necessary to understand how such events could affect the neutral density and photochemistry in the lower altitudes. Further studies could shed light into possible precipitation events and dynamics and their impacts on the energetics and dynamics of the lower thermospheric region.

[22] Note that the latitudinal coverage for the Northern and Sothern hemisphere used in Figure 8 are not uniform for all the observations, with the scans sometimes limited to about 5–20°S during the Northern winter and equinox months, while in most of the cases the scans cover beyond 30°N. This might bias the distribution of the O(^{1}D) peaks with respect to the equator, especially if some of the O(^{1}D) enhancements are related to the meridional wind abatement or reversal around midnight, which occurs more in the summer hemisphere [*Burnside and Tepley*, 1990]. The altitude of the plasma density modulation is also important in the production of O(^{1}D) intensity. If the plasma enhancement is above 300–350 km altitude, it will have less effect on the O(^{1}D) 630.0 nm emission. Such factors might be responsible for the lesser frequency of the observed O(^{1}D) enhancements in the Southern hemisphere. The differences in the latitudinal distribution of the O(^{1}D) and OH(9–3) enhancements could be related to the different processes controlling them. However, there is lack of enough observations in the Southern latitudes to comment on such differences, especially near 20°S. Further analysis with more observations over all the satellite tracks, uniformly covering both the hemispheres, is required to understand the latitudinal and longitudinal distribution of the enhancements.

[23] In conclusion, the enhancements in the ISUAL 630.0 nm limb images near the equatorial region comes from the nighttime ionization, while the atmospheric dynamics and/or energetic particle precipitation could cause such features in the midlatitudes and also in the SAA region. The results demonstrate the potential of ISUAL limb images in investigating both neutral and charged particle precipitation events and the global coverage provides the opportunity to study large-scale structures such as TID, and dynamics related to neutral wind, tides, gravity waves, etc., using their airglow signatures.

[24] **Acknowledgments.** The authors are thankful to the reviewers for their comments and suggestions that have helped to improve the presentation of the manuscript. This work is supported by National Space Organization grant 98-NSPO(B)-IC-FA07-01(L) and National Science Council grant NSC97-2628-M-008-003 to National Central University, as well as National Space Organization grant 98-NSPO(B)-ISUAL-FA09-01 to National Cheng Kung University, Taiwan.

[25] Zuyin Pu thanks Hisao Takahashi and another reviewer for their assistance in evaluating this paper.

References

Adachi, T., H. Fukunishi, Y. Takahashi, Y. Hiraki, R.-R. Hsu, H.-T. Su, A. B. Chen, S. B. Mende, H. U. Frey, and L. C. Lee (2006), Electric field transition between the diffuse and streamer regions of sprites estimated from ISUAL/array photometer measurements, *Geophys. Res. Lett.*, *33*, L17803, doi:10.1029/2006GL026495.

Baker, D. N., J. B. Blake, D. J. Gorney, P. R. Higbie, R. W. Klebesade, and J. H. King (1987), Highly relativistic magnetospheric electrons: A role in coupling to the middle atmosphere, *Geophys. Res. Lett.*, *14*, 1027–1030, doi:10.1029/GL014i010p01027.

Bilitza, D. (2001), International Reference Ionosphere 2000, *Radio Sci.*, *36*, 261–275, doi:10.1029/2000RS002432.

Bittencourt, J. A., and Y. Sahai (1979), Behavior of the [OI]6300 Å emission at the magnetic equator and its reaction to the vertical $E \times B$ drift velocity, *J. Atmos. Terr. Phys.*, *41*, 1233–1239, doi:10.1016/0021-9169(79)90026-6.

Bowman, G. G. (1977), Low-latitude ionospheric height changes associated with geomagnetic substorms, *J. Atmos. Terr. Phys.*, *39*, 1169–1173, doi:10.1016/0021-9169(77)90025-3.

Burnside, R. G., and C. A. Tepley (1990), Airglow intensities observed in the southern and northern hemispheres, *Planet. Space Sci.*, *38*, 1161–1177, doi:10.1016/0032-0633(90)90024-K.

Burnside, R. G., J. W. Meriwether, and M. R. Torr (1977), Contamination of ground-based measurements of OI (6300 Å) and NI (5200 Å) airglow by OH emissions, *Planet. Space Sci.*, *25*, 985–988, doi:10.1016/0032-0633(77)90012-5.

Chakrabarti, S. (1998), Ground based spectroscopic studies of sunlit airglow and aurora, *J. Atmos. Sol. Terr. Phys.*, *60*, 1403–1423, doi:10.1016/S1364-6826(98)00060-1.

Chern, J. L., R. R. Hsu, H. T. Su, S. B. Mende, H. Fukunishi, Y. Takahashi, and L. C. Lee (2003), Global survey of upper atmospheric transient luminous events on the ROCSAT-2 satellite, *J. Atmos. Sol. Terr. Phys.*, *65*, 647–659, doi:10.1016/S1364-6826(02)00317-6.

Chu, F. D., J. Y. Liu, H. Takahashi, J. H. A. Sobral, M. J. Taylor, and A. F. Medeiros (2005), The climatology of ionospheric plasma bubbles and irregularities over Brazil, *Ann. Geophys.*, *23*, 379–384.

Colerico, M., M. Mendillo, D. Nottingham, J. Baumgardner, J. Meriwether, J. Mirick, B. W. Reinisch, J. L. Scali, C. G. Fesen, and M. A. Biondi (1996), Coordinated measurements of *F* region dynamics related to the thermospheric midnight temperature maximum, *J. Geophys. Res.*, *101*(A12), 26,783–26,793, doi:10.1029/96JA02337.

DeMajistre, R., P. Brandt, T. J. Immel, J.-H. Yee, A. Dalgarno, L. J. Paxton, and V. A. Kharchenko (2005), Storm-time enhancement of mid-latitude ultraviolet emissions due to energetic neutral atom precipitation, *Geophys. Res. Lett.*, *32*, L15105, doi:10.1029/2005GL023059.

Dmitriev, A., and H.-C. Yeh (2008), Storm-time ionization enhancements at the topside low-latitude ionosphere, *Ann. Geophys.*, *26*, 867–876.

Fagundes, P. R., Y. Sahai, I. S. Batista, M. A. Abdu, J. A. Bittencourt, and H. Takahashi (1999), Observations of day-to-day variability in precursor signatures to equatorial *F* region plasma depletions, *Ann. Geophys.*, *17*, 1053–1063, doi:10.1007/s00585-999-1053-x.

Greenspan, J. A. (1966), Synoptic description of the 6300 Å nightglow near 78° west longitude, *J. Atmos. Terr. Phys.*, *28*, 739–745, doi:10.1016/0021-9169(66)90022-5.

Hedin, A. E. (1991), Extension of the MSIS thermosphere model into the middle and lower atmosphere, *J. Geophys. Res.*, *96*, 1159–1172, doi:10.1029/90JA02125.

Herrero, F. A., and J. W. Meriwether Jr. (1980), 6300-Å airglow meridional intensity gradients, *J. Geophys. Res.*, *85*, 4191–4204, doi:10.1029/JA085iA08p04191.

Hocke, K., and K. Schlegel (1996), A review of atmospheric gravity waves and travelling ionospheric disturbances: 1982–1995, *Ann. Geophys.*, *14*, 917–940.

Kelley, M. C., J. J. Makela, B. M. Ledvina, and P. M. Kintner (2002), Observations of equatorial spread F from Haleakala, Hawaii, *Geophys. Res. Lett.*, *29*(20), 2003, doi:10.1029/2002GL015509.

Kuo, C.-L., R. R. Hsu, A. B. Chen, H. T. Su, L. C. Lee, S. B. Mende, H. U. Frey, H. Fukunishi, and Y. Takahashi (2005), Electric fields and electron energies inferred from the ISUAL recorded sprites, *Geophys. Res. Lett.*, *32*, L19103, doi:10.1029/2005GL023389.

Lin, C. S., and H. C. Yeh (2005), Satellite observations of electric fields in the South Atlantic anomaly region during the July 2000 magnetic storm, *J. Geophys. Res.*, *110*, A03305, doi:10.1029/2003JA010215.

Link, R., and L. L. Cogger (1988), A reexamination of the OI 6300 Å nightglow, *J. Geophys. Res.*, *93*(A9), 9883–9892, doi:10.1029/JA093iA09p09883.

Liu, N., et al. (2006), Comparison of results from sprite streamer modeling with spectrophotometric measurements by ISUAL instrument on FORMOSAT-2 satellite, *Geophys. Res. Lett.*, *33*, L01101, doi:10.1029/2005GL024243.

Lopez-Gonzalez, M. J., E. Rodriguez, G. G. Shepherd, S. Sargoytchev, M. G. Shepherd, V. M. Aushev, S. Brown, M. Garcia-Comas, and R. H. Wiens (2005), Tidal variations of O_2 Atmospheric and OH (6–2) airglow and temperature at mid-latitudes from SATI observations, *Ann. Geophys.*, *23*, 3579–3590.

Makela, J. J., B. M. Ledvina, M. C. Kelley, and P. M. Kintner (2004), Analysis of the seasonal variations of equatorial plasma bubble occurrence observed from Haleakala Hawaii, *Ann. Geophys.*, *22*, 3109–3129.

Makhlouf, U. B., R. H. Picard, and J. R. Winick (1995), Photochemical-dynamical modeling of the measured response of airglow to gravity waves: 1. Basic model for OH airglow, *J. Geophys. Res.*, *100*(D6), 11,289–11,311, doi:10.1029/94JD03327.

Martinis, C., J. V. Eccles, J. Baumgardner, J. Manzano, and M. Mendillo (2003), Latitude dependence of zonal plasma drifts obtained from dual-site airglow observations, *J. Geophys. Res.*, *108*(A3), 1129, doi:10.1029/2002JA009462.

Mende, S. B., G. R. Swenson, and S. P. Geller (1993), Limb view spectrum of the Earth's airglow, *J. Geophys. Res.*, *98*(A11), 19,117–19,125, doi:10.1029/93JA02282.

Mendillo, M., and J. Baumgardner (1982), Airglow characteristics of equatorial plasma depletions, *J. Geophys. Res.*, *87*, 7641–7652, doi:10.1029/JA087iA09p07641.

Mendillo, M., E. Zesta, S. Shodhan, P. J. Sultan, R. Doe, Y. Sahai, and J. Baumgardner (2005), Observations and modelling of the coupled latitude-altitude patterns of equatorial plasma depletions, *J. Geophys. Res.*, *110*, A09303, doi:10.1029/2005JA011157.

Mukherjee, G. K. (2003), Studies of the equatorial *F* region depletions and dynamics using multiple wavelength nightglow imaging, *J. Atmos. Sol. Terr. Phys.*, *65*, 379–390, doi:10.1016/S1364-6826(02)00214-6.

Nelson, G. J., and L. L. Cogger (1971), Dynamical behavior of the nighttime ionosphere at Arecibo, *J. Atmos. Terr. Phys.*, *33*, 1711–1726, doi:10.1016/0021-9169(71)90219-4.

Peterson, V. L., T. E. Van Zandt, and R. B. Norton (1966), *F* region nightglow emissions of atomic oxygen: 1. Theory, *J. Geophys. Res.*, *71*, 2255–2265.

Pimenta, A. A., P. R. Fagundes, Y. Sahai, J. A. Bittencourt, and J. R. Abalde (2003), Equatorial *F* region plasma depletion drifts: Latitudinal and seasonal variations, *Ann. Geophys.*, *21*, 2315–2322.

Rajesh, P. K., J. Y. Liu, H. S. S. Sinha, S. B. Banerjee, R. N. Misra, N. Dutt, and M. B. Dadhania (2007), Observations of plasma depletions in 557.7 nm over Kavalur, *J. Geophys. Res.*, *112*, A07307, doi:10.1029/2006JA012055.

Roelof, E. C. (1987), Energetic neutral atom image of a storm-time ring current, *Geophys. Res. Lett.*, *14*, 652–655, doi:10.1029/GL014i006p00652.

Sahai, Y., J. Aarons, M. Mendillo, J. Baumgardener, J. A. Bittencourt, and H. Takahashi (1994), OI 630 nm imaging observations of equatorial plasma depletions at 16° dip latitude, *J. Atmos. Terr. Phys.*, *56*(11), 1461–1475, doi:10.1016/0021-9169(94)90113-9.

Sahai, Y., P. R. Fagundes, and J. A. Bittencourt (2000), Transequatorial *F* region ionospheric plasma bubbles: Solar cycle effects, *J. Atmos. Sol. Terr. Phys.*, *62*, 1377–1383, doi:10.1016/S1364-6826(00)00179-6.

Scheer, J., and E. R. Reisen (1998), Extreme intensity variations of O_2b airglow induced by tidal oscillations, *Adv. Space Res.*, *21*(6), 827–830, doi:10.1016/S0273-1177(97)00682-0.

Shepherd, G. G., T. Fancott, J. McNally, and H. S. Kerr (1973), ISIS-II atomic oxygen red line photometer, *Appl. Opt.*, *12*(8), 1767–1774, doi:10.1364/AO.12.001767.

Shepherd, G. G., J. Stegman, P. Espy, C. McLandress, G. Thuillier, and R. H. Wiens (1999), Springtime transition in lower thermospheric atomic oxygen, *J. Geophys. Res.*, *104*(A1), 213–223, doi:10.1029/98JA02831.

Shiokawa, K., C. Ihara, Y. Otsuka, and T. Ogawa (2003), Statistical study of nighttime medium-scale traveling ionospheric disturbances using midlatitude airglow images, *J. Geophys. Res.*, *108*(A1), 1052, doi:10.1029/2002JA009491.

Sinha, H. S. S., P. K. Rajesh, R. N. Misra, R. Pandey, N. Dutt, M. B. Dadhania, and S. B. Banerjee (2003), Imagenes opticas de las disminuciones de plasma en la cresta de la anomalia ecuatorial, *Rev. Boliv. Fis.*, *9*, 52–59.

Swenson, G. R., S. B. Mende, and E. J. Llewellyn (1989), Imaging observations of lower thermospheric $O(^1S)$ and O_2 airglow emissions from STS-9: Implications of height variations, *J. Geophys. Res.*, *94*, 1417–1429, doi:10.1029/JA094iA02p01417.

Takahashi, H., Y. Sahai, B. R. Clemesha, P. P. Batista, and N. R. Teixeria (1977), Diurnal and seasonal variations of the OH(8,3) airglow band and its correlation with OI 5577 Å, *Planet. Space Sci.*, *25*, 541–547, doi:10.1016/0032-0633(77)90060-5.

Takahashi, H., Y. Sahai, B. R. Clemesha, and P. P. Batista (1984), Tidal and solar cycle effects on the OI 5577Å, NaD, and OH(8,3) airglow emissions observed at 23°S, *Planet. Space Sci.*, *32*(7), 897–902, doi:10.1016/0032-0633(84)90013-8.

Takahashi, H., P. P. Batista, R. A. Buriti, D. Gobbi, T. Nakamura, T. Tsuda, and S. Fukao (1999), Response of the airglow OH emission, temperature and mesopause wind to the atmospheric wave propagation over Shigaraki, Japan, *Earth Planets Space*, *51*, 863–875.

Taylor, M. J., J. V. Eccles, J. Labelle, and J. H. A. Sobral (1997), High-resolution OI(630 nm) image measurements of *F* region depletion drifts during the Guara campaign, *Geophys. Res. Lett.*, *24*, 1699–1702, doi:10.1029/97GL01207.

Thuillier, G., J. W. King, and A. J. Slater (1976), An explanation of the longitude variation of the $O(^1D)$ 630 nm tropical nightglow intensity, *J. Atmos. Terr. Phys.*, *38*, 155–158, doi:10.1016/0021-9169(76)90123-9.

Thuillier, G., R. H. Wiens, G. G. Shepherd, and R. G. Roble (2002), Photochemistry and dynamics in thermospheric intertropical arcs measured by the WIND Imaging Interferometer on board UARS: A comparison with TIE-GCM simulations, *J. Atmos. Sol. Terr. Phys.*, *64*, 405–415, doi:10.1016/S1364-6826(01)00109-2.

Tinsley, B. A., R. P. Rohbaugh, M. Ishimoto, M. R. Torr, and D. G. Torr (1994), Middle- and low-latitude emissions from energetic neutral atom precipitation seen from ATLAS 1 under quiet magnetic conditions, *J. Geophys. Res.*, *99*(A10), 19,577–19,584, doi:10.1029/94JA01265.

Torr, M. R., and D. G. Torr (1984), Energetic oxygen in mid-latitude aurora, *J. Geophys. Res.*, *89*(A7), 5547–5553, doi:10.1029/JA089iA07p05547.

Torr, M. R., D. G. Torr, and R. R. Laher (1985), The O_2 atmospheric 0–0 band and related emissions at night from Spacelab-I, *J. Geophys. Res.*, *90*, 8525–8538, doi:10.1029/JA090iA09p08525.

Weber, E. J., J. Buchau, R. H. Eather, and S. B. Mende (1978), North-south aligned equatorial depletions, *J. Geophys. Res.*, *83*, 712–716, doi:10.1029/JA083iA02p00712.

Wiens, R. H., S. Habtemichael, F. Andemariam, K. Welday, J. Criswick, S. Brown, and S. Sargoytchev (2004), Brightness variation of the northern 630 nm intertropical arc and the midnight pressure bulge over Eritrea, *Ann. Geophys.*, *22*, 3251–3259.

Zhang, S. P., R. G. Roble, and G. G. Shepherd (2001), Tidal influence on the oxygen and hydroxyl nightglows: Wind Imaging Interferometer observations and thermosphere/ionosphere/mesosphere electrodynamics general circulation model, *J. Geophs. Res.*, *106*, 21,381–21,393.

A. B. Chen, C. Y. Chiang, M.-L. Hsu, R. R. Hsu, C. H. Lin, and H. T. Su, Department of Physics, National Cheng Kung University, 1 Ta-Hsueh Road, Tainan, 70101, Taiwan.

W. S. Chen, J. Y. Liu, and P. K. Rajesh, Institute of Space Science, National Central University, 300 Jhongda Road, Chung-Li, 32001, Taiwan. (jyliu@jupiter.ss.ncu.edu.tw)

J. B. Nee, Department of Physics, National Central University, 300 Chung Ta Street, Chung-Li, 32054, Taiwan.

J. H. Yee, Johns Hopkins University Applied Physics Laboratory, 11100 Johns Hopkins Road, Laurel, MD 20723-6005, USA.